

Material flow during friction hydro-pillar processing

Renan Landell, Luis Fernando Kanan, Diogo Buzzatti, Buchibabu Vicharapu, Amitava De & Thomas Clarke

To cite this article: Renan Landell, Luis Fernando Kanan, Diogo Buzzatti, Buchibabu Vicharapu, Amitava De & Thomas Clarke (2020) Material flow during friction hydro-pillar processing, Science and Technology of Welding and Joining, 25:3, 228-234, DOI: [10.1080/13621718.2019.1679963](https://doi.org/10.1080/13621718.2019.1679963)

To link to this article: <https://doi.org/10.1080/13621718.2019.1679963>



Published online: 17 Oct 2019.



Submit your article to this journal [↗](#)



Article views: 246



View related articles [↗](#)





View Crossmark data [↗](#)



Citing articles: 4 View citing articles [↗](#)

Material flow during friction hydro-pillar processing

Renan Landell^a, Luis Fernando Kanan^a, Diogo Buzzatti^a, Buchibabu Vicharapu ^b, Amitava De ^b and Thomas Clarke^a

^aPhysical Metallurgy Laboratory (LAMEF) – PPG3M/UFRGS, Porto Alegre, Brazil; ^bIndian Institute of Technology Bombay, Mumbai, India

ABSTRACT

Friction hydro-pillar processing (FHPP) is a novel technique that involves solid-state joining of an external plug onto a substrate by plastic deformation. A systematic investigation on material flow during FHPP is required but rarely reported. The present work reports a coupled theoretical and a three-dimensional X-ray computer tomography-based experimental study using a Ti-alloy as a tracer material to realise the material flow during FHPP of a AISI 4140 steel substrate. The cumulative results showed that the central portion of the plug deformed in a series of layer-wise shear planes. However, the plasticised material towards the outer area of the plug flowed through the clearance between the plug and the substrate with excess volume moving out as flash.

ARTICLE HISTORY

Received 21 July 2019
Revised 1 October 2019
Accepted 6 October 2019

KEYWORDS

Friction welding; friction hydro-pillar processing; friction taper plug welding; material flow; X-ray computer tomography; numerical simulation; AISI 4140 steel; Ti–6Al–4V

Introduction

Friction hydro-pillar processing (FHPP) is a solid-state process, which involves joining of an external solid plug (referred to as stud) into a thick metallic base in order to repair cracks. FHPP is, therefore, finding increasing applications in oil, gas and power plant piping's, and parts and components in shipping fabrications [1–3]. FHPP avoids common welding problems associated with melting of materials in weld zone and HAZ such as porosity, hydrogen embrittlement and residual stresses [1,4]. The process starts with the scraping of the crack and adjacent material from the damaged component by machining to form a shaped, blind hole with a base. A rotating, pre-shaped stud of similar chemical composition is then forced into the hole resulting in flow of plasticised stud material filling the hole. Subsequent coalescence of plasticised material with the substrate completes the process and brings back the damaged part to service. Figure 1 schematically shows three sequential steps of FHPP. The 'dwell stage' completes when the rotating stud touches the base of the crack opening in the substrate and marks the beginning of frictional heating along the stud-substrate interface. The plasticised material fills the hole in the 'burn-off stage'. The 'forging stage' begins with the stoppage of the stud rotation and application of additional force to facilitate consolidation of the plasticised material with the substrate [5,6].

FHPP has been conceived initially with straight cylindrical-shaped studs [1,7]. Meyer [1] studied the material flow in FHPP of X65 pipeline steel using nickel

as a tracer material that sheared-off during the burn-off stage due to overlapping and competing friction planes. The straight cylindrical-shaped studs also showed inadequate mixing and lack of coalescence with the substrate [1]. Subsequent use of tapered cylindrical studs improved the filling of crack volumes and consolidation processes in FHPP of C–Mn steel, AISI 4140 and duplex stainless steels (UNS S31803) [5–8]. The taper cylindrical studs also enhanced the rate of frictional heat generation [5,9]. The lack of bonding defect could also be reduced by using pre-machined profiles of the existing cracks with chamfered edges [4]. Yin et al. [9] reported brittle microstructure of the welded region in underwater FHPP of X65 pipeline steel and attributed the same to high cooling rate. In summary, taper cylindrical studs and pre-machined cracks with chamfered edges provided improved joint in FHPP although the selection of appropriate processing conditions remained a challenge.

The key processing conditions in FHPP include the rotational speed of the stud, the peak force and the rate at which the force is applied on the stud, and the burn-off length of the stud. Kanan et al. [6] could ensure filling of the crack-hole with plasticised material by a gentler increase in the stud force with time and using a longer dwell period in FHPP of AISI 4140 steel. The authors argued that a longer dwell period allowed adequate thermal softening and improved flow of plasticised stud material. In contrast, Vicharapu et al. [5] and Yin et al. [9] noted that a higher axial force could reduce the overall processing time at the cost of high

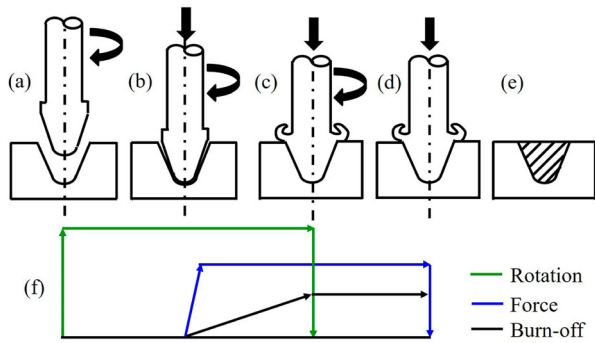


Figure 1. Schematic illustrating (a) Initial stage, (b) dwell stage, (c) burn-off stage, (d) forging stage during friction stir hydro-pillar processing. Figure 1(f) shows schematically the variation of stud rotation, axial force, and stud burn-off at each stage.

cooling rates and joint hardness. The effect of stud force on joint properties was found sensitive to the stud-hole geometries [2,10]. Cui et al. [11] opined that suitable combinations of stud rotational speed and force could improve the material flow and filling of crack-hole. However, these studies remained speculative about the influence of processing conditions and stud-hole geometry on material flow as a direct investigation of material flow in FHPP was not attempted.

Attempts to examine material flow in FHPP using tracer material are reported in recent times while these were limited to the sectional views from the metallographic observations in two-dimensional planes only [1,9]. The non-destructive X-ray computer tomography (XCT) technique has become a popular tool for the acquisition of three-dimensional (3D) images in processing of a wide range of engineering materials [12]. XCT technology was employed for 3D visualisation of porosity and volumetric welding defects [13,14], and distribution of intermetallic compounds in multi-material joining [15]. Such studies are important in understanding the material flow during FHPP, but not available in open literature yet.

The present work aims at probing the stud material flow in FHPP of AISI 4140 with a tracer material and employing both XCT analysis and metallographic characterisations. Cylindrically shaped tracer material rods were inserted inside the stud to visualise the material flow explicitly. A finite element based fully coupled temperature-displacement analysis of FHPP is undertaken. The numerically computed peak temperature, material flow, flash volume and the weld shape are compared with the corresponding XCT and metallographic observations.

Experimental procedure

The FHPP experiments were conducted using a tapered stud and a thick substrate of AISI 4140 at the Physical Metallurgy Laboratory (LAMEF), Department of Metallurgical Engineering, Federal University of

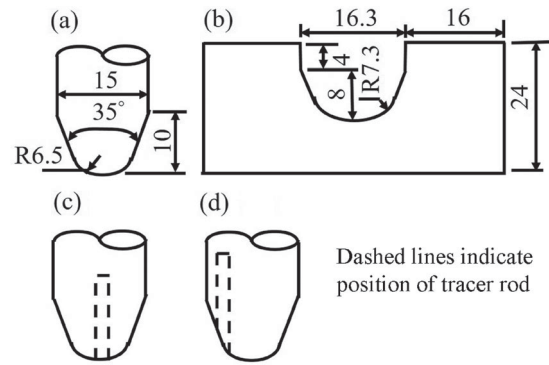


Figure 2. Schematic view of (a) stud, (b) substrate with crack-hole, and (c-d) stud with tracer insert rods – (c) tracer located centrally, and (d) tracer offset by 4 mm.

Table 1. Chemical composition of AISI 4140 steel.

C	Cr	Mo	Si	P	S	Mn	Ni
0.4	0.9	0.2	0.2	0.01	0.01	0.85	< 0.005

Rio Grande Do Sul (UFRGS), Brazil. Titanium alloy, Ti-6Al-4V was used as a tracer material due to its identical thermo-mechanical behaviour with that of AISI 4140. Figure 2 shows the original stud and substrate geometry. Table 1 shows the chemical composition of the stud and substrate material. The nature of variation of flow stress of the stud and the tracer alloys are presented in Appendix. The process conditions include the stud force, rotational speed and burn-off length of 35 kN, 7000 rev min⁻¹ and 7 mm, respectively. A set of trial experiments were conducted initially to ensure that the considered process condition could provide sound joints with adequate properties without any tracer material. Figure 2 shows two distinct locations for the placement of tracer rods of diameter 2 mm each inside the stud. It is presumed that the tracer material at the stud centre would experience zero tangential velocity while that in the stud periphery undergo the maximum tangential velocity. Three different experiments were conducted with (i) original stud, and (ii-iii) the stud with Ti-6Al-4V tracer at (ii) stud centre, and (iii) 4 mm offset from the stud centre.

XCT analysis was performed on FHPP samples to study the material flow by a Phoenix V/TOME/XM[®] manufactured by General Electric (GE)[®]. The welded coupons were machined to 21 mm diameter cylindrical rods for XCT scanning according to the machine specifications [16]. The samples were prepared with adequate care to maintain the FHPP joint at the central location of the rod. The voltage and current for the XCT analysis were 210 kV and 190 mA, respectively. The post-processing of XCT scans was performed using an open source software, 'Voreen Rendering', from the University of Munster, Germany, to visualise the 3D distribution of tracer material [17]. The optical microscopy (OM) analysis was also performed on joint

cross-sections (after etching with 5% nital solution) to view the tracer material distribution. Two separate sample joints were made for XCT and OM analyses.

Numerical modelling

The fully coupled temperature-displacement analysis of FHPP process is undertaken using the finite element software ABAQUS®/Standard V6.14 [18]. The analysis considers the rate of heat generation due to frictional heating along the stud-substrate interface and plastic deformation of stud material. Figure 3(a) schematically shows the stud – substrate assembly with the stud modelled as an inverted taper cylindrical frustum with hemi-spherical end. Both the stud and substrate are considered as deformable and discretised with the special axisymmetric element (CGAX4HT) that includes temperature, displacement and twist degrees of freedom [19,20]. The twist degree of freedom allows the rotation and shear deformation in the out-of-plane direction. The governing heat transfer equation in two-dimensional cylindrical coordinate system can be stated as

$$\frac{1}{r} \frac{\partial}{\partial r} \left(kr \frac{\partial T}{\partial r} \right) + \frac{\partial}{\partial z} \left(k \frac{\partial T}{\partial z} \right) = \rho C_p \frac{\partial T}{\partial t} \quad (1)$$

where k , ρ , C_p , T and t referred to the thermal conductivity, density, specific heat, and temperature and time variable, respectively. The boundary conditions can be expressed as

$$q_s - k \frac{\partial T}{\partial n} - h = 0 \quad (2)$$

where h is the convective heat transfer coefficient and q_s is the rate of frictional heat generation along the stud-substrate interface that is estimated as

$$q_s = \eta_h r \omega \tau \quad (3)$$

$$\tau = \begin{cases} \tau_y; & \tau_y \leq P\mu \\ P\mu; & \tau_y > P\mu \end{cases} \quad (4)$$

where η_h is the fractional heat transferred to stud, r is the radial distance of a point from the stud axis, and μ , ω , P and τ_y refer to the co-efficient of friction, angular speed of stud, axial pressure on the stud and shear yield stress of stud material, respectively. The values of η_h and μ were considered as 0.5 and 0.3, respectively [5,6]. A lumped expression is used to estimate the convective heat loss from the surfaces as [21,22]

$$h = h_b \times (T - T_0) \quad (5)$$

where $h_b = 10.0 \text{ W m}^{-2} \text{ K}^{-1}$.

The analysis of mechanical response follows Equation (6)

$$K \times U = F_M \quad (6)$$

where K , U and F_M are the stiffness matrix, displacement vector and the force vector due to mechanical

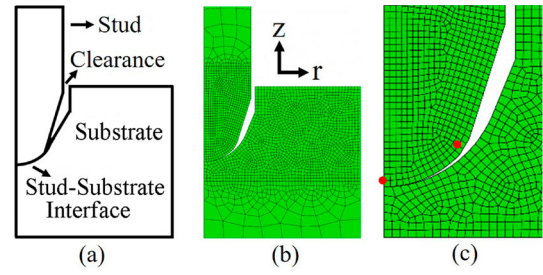


Figure 3. Schematic of the (a) stud and substrate assembly, and (b) initial mesh and (c) initial tracer locations (indicated in red colour) at the beginning of the stud burn-off stage.

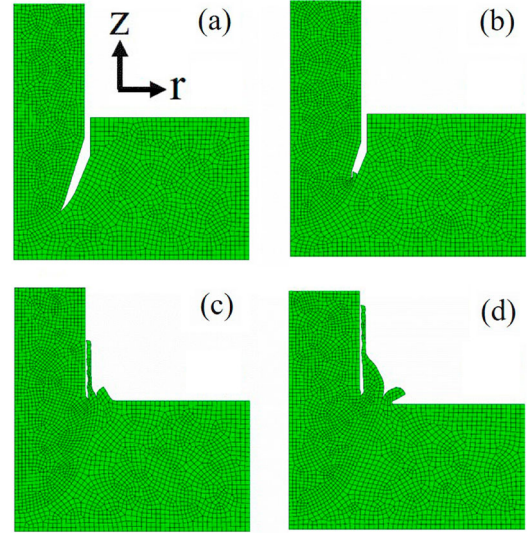


Figure 4. Re-meshed stud-substrate assembly at stud burn-off length (mm) of (a) 0.25, (b) 2, (c) 6, and (d) 7 during stud burn-off.

work, respectively. The non-linearity in the mechanical analysis arises out of simultaneous displacement and rotation of the stud, and the temperature-dependent thermo-physical properties of the stud and substrate material. The substrate bottom surface is constrained in all the directions. The stud is set to rotate with an angular velocity of ' ω ' in radial direction and displace in negative Z-direction during the stud burn-off.

Figure 3(b) shows the initial discretised stud-substrate assembly. The elements along the stud-substrate interface undergo large deformation as the modelling calculation continues through the burn-off stage. Significant distortion in element shapes tends to terminate the calculation process frequently and, intermittent re-meshing of heavily distorted elements is needed. A python-based script was therefore written to undertake automatic remeshing of distorted elements and remapping of nodal solutions after each time-step [18]. Figure 4(a–d) shows typical remeshed discretised geometry at four different time-steps during the stud burn-off period. The total number of elements was increased from 2982 to 3043 in Figure 4(a–d), respectively. The remeshing process was undertaken sixty times to simulate 7 mm stud burn-off length for the given process conditions and stud-substrate geometry.

Table 2. Material properties of AISI 4140 [6].

Density (kg m ⁻³)	7830
Solidus temperature (K)	1750
Thermal conductivity (W mK ⁻¹)	$54.91 - 3.33e^{-2} \times T + 1.0e^{-5} \times T^2$ for $T < 1200$ K 30.0 for $T \geq 1200$ K
Specific heat (J kgK ⁻¹)	$361.55 + 1.13e^{-1} \times T + 3.0e^{-4} \times T^2$ for $T \leq 1200$ K 607.0 for $T > 1200$ K

Table 3. Johnson-Cook material model constants for AISI 4140 [23].

Material	A (MPa)	B (MPa)	C	M	N	T _M (K)
AISI 4140	595	580	0.023	1.03	0.133	1820

Note: A: Initial yield stress, B: Hardening modulus, C: Strain rate dependence coefficient, M: thermal softening coefficient, N: strain-hardening coefficient, T_M: Melting temperature.

The material flow during FHPP was modelled with the help of tracer particle tracking technique available in ABAQUS[®]. The tracer particles were located slightly above the stud surface inside the stud as shown in Figure 3(c) (highlighted with red colour). Table 2 shows the thermo-physical properties and Table 3 presents the Johnson-Cook material constants for the estimation of flow stress of AISI 4140. The computed peak temperature, material flow, flash volume and the weld shape are compared with the corresponding experimental results.

Results and discussion

Figure 5 shows the joint cross-sections without (Figure 5(a)) and with Ti-6Al-4V tracer materials (Figure 5(b,c)). The joint in Figure 5(b) corresponds to the stud with a central tracer (Figure 2(c)) and that in Figure 5(c) with the tracer at a slightly offset location inside the stud (Figure 2(d)). Figure 5(b,c) shows the presence of Ti-6Al-4V tracer (brighter regions) at the centre and along the stud-substrate interface, respectively. The joint cross-sections in Figure 5(a-c) show nearly identical profile with little presence of micro-crack and unbonded flash indicated by the red arrows and square boxes. The excess portion above the substrate surface is not part of the joint and removed later. A magnified view of the deformed tracer rod (Figure 5(b)) is shown in Figure 5(d) that manifests thin occasional overlapping layers of tracer material flowing along the stud-substrate interface. These layers are presumed as the representative shear layers. Similar layers were noted earlier in FHPP of X65 pipeline steel [1]. Figure 5(e) presents a zoomed view of Figure 5(c) with greater clarity depicting a radially outward, nearly uniform flow of tracer material through the stud-substrate interface with no presence of tracer in the central region of the interface. This indicates a similar nature of radially outward and then, upward flow of the plasticised stud material from its peripheral region through the stud-substrate interface. A further detailed visualisation of the flow of tracer material is presented through the XCT analysis subsequently.

Figure 6 shows the XCT images of the joints when the Ti-6Al-4V tracer was at the stud centre (Figure 6(a,b)) and slightly offset from the stud centre (Figure 6(c,d)). The fine dark particles in the processed zones indicate the distribution of tracer elements. Figure 6(b) shows a magnified view of Figure 6(a) near to the bottom of the deformed tracer rod. The intermittent ring patterns shown in Figure 6(b) indicate the typical shear layers that corroborates well with the metallographic observation (Figure 5(d)). The offset placement of the tracer rod inside the stud led to the twisting of the rod as shown in Figure 6(c). A zoomed view of Figure 6(c) in Figure 6(d) indicates a radially outward flow of the tracer elements – upward through the stud-substrate interface as also observed in direct metallographic observation (Figure 5(e)). The Ti-6Al-4V tracer distributions in Figure 6(d) appear to be slightly intermittent that is attributed to insufficient resolution of the XCT setup to view finer tracer particles. The dark circular patterns along the top surface in Figure 6(a-c) depict unbonded flash material. The optical images (Figure 5) only show the tracer distribution along the sectioned plane, whereas XCT analysis (Figure 6) reveals the tracer distribution in a 3D space, hence providing a better visualisation. Overall, both the XCT and metallographic observations indicate that the central section of the stud deforms plastically in a series of shear planes and fills up the crack-hole. The plasticised material towards the stud periphery flows through the stud-substrate interface thereby completing the filling process along the crack-hole profile.

Numerical results

Figure 7 shows the computed temperature iso-therms at four time-steps during the stud burn-off stage. An initial stud burn-off of around 0.5 mm occurred at a time instant of 0.9 s. The peak temperature at the end of the same time-instant reached to around 1025 K primarily due to frictional heat generation along the stud-substrate interface at the bottom of the stud (Figure 7(a)). Only a little advancement of the plasticised stud material through the stud-substrate interface is noted in Figure 7(a). Figure 7(b) shows the temperature distribution and further advancement of plasticised stud material through the stud-substrate interface after the stud burn-off length reached to 2 mm. The corresponding time instant was 4 s. A rise in the peak temperature to around 1275 K is noted in Figure 7(b). The increase in stud burn-off from 2 to 6 mm at a time instant of 14 s has led to the complete filling of the crack-hole with the peak temperature reaching around 1500 K along the stud-substrate interface. Further forcing the stud burn-off up to 7 mm has resulted in flash coming out from the crack-hole as shown in Figure 7(d). The computed peak temperatures reported in Figure 7 varies between 0.7 and 0.84 times the solidus temperature (T_S)

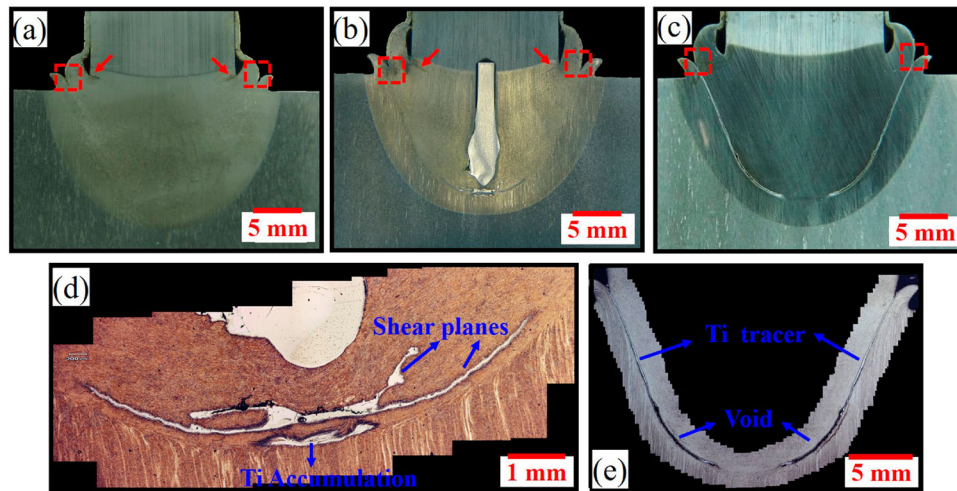


Figure 5. Post weld macrographs of joint cross-sections with (a) no tracer, (b) Ti-6Al-4V tracer at centre of the stud, (c) Ti-6Al-4V tracer at 4 mm away from the stud centre. Figure 5(d,e) shows magnified views of Figure 5(b,c), respectively.

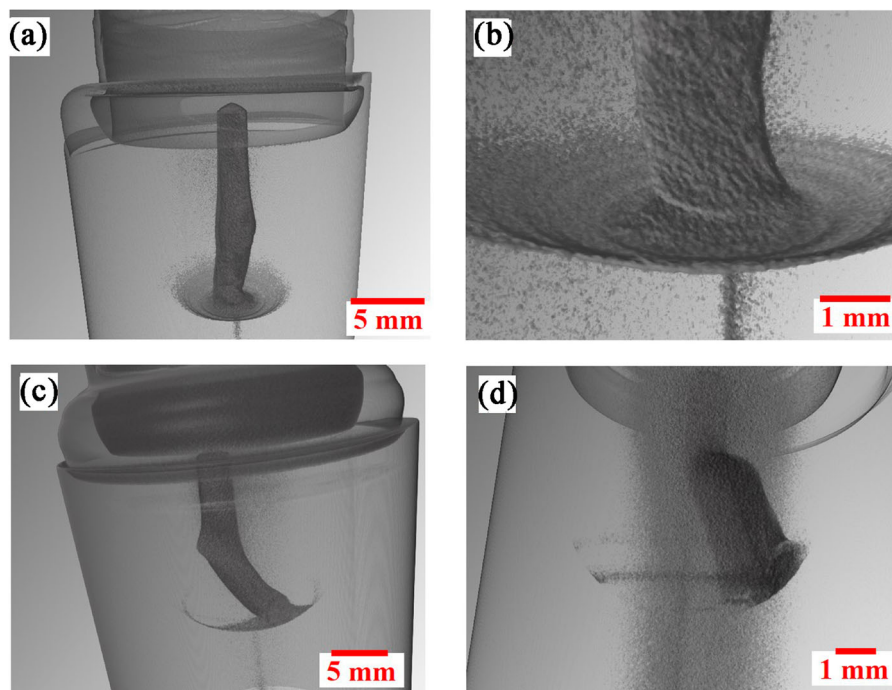


Figure 6. XCT images with Ti-6Al-4V tracer rod at the (a) stud centre, and (b) a zoomed view of the same, (c) and (d) are with the Ti-6Al-4V tracer rod at a 4 mm offset from the stud centre and its magnified view, respectively.

of the workpiece material (ref Table 2). Previous studies on FHPP of AISI 4140 [6] and of ASTM A36 steel [5] reported similar range of computed peak temperature. The stud burn-off length of around 5 mm filled the crack-hole completely and further introduction of the stud has led to flash (Figure 7(c-d)). The computed results are checked further with the measured material flow and joint shape.

Computed material flow and joint and flash formation

Figure 8(a,b) shows the step by step spatial evolution of tracer particle (highlighted in red colour) as the FHPP process progresses with increase in the stud

burn-off length. The initial and final tracer locations before and after the stud burn-off stage are indicated by the terms 'Start' and 'End', respectively. The locus of the tracer particle shown in Figure 8(a) depicts the movement of the shear plane that is in line with both the XCT and metallographic observations (ref. Figures 5(d) and 6(b)). Likewise, the computed tracer distribution shown in Figure 8(b) from the offset placement of the tracer agreed well with the corresponding experimentally measured results (ref. Figures 5(e) and 6(d)). The model is therefore considered fairly representative in realising the flow and expelling of stud material as flash through stud-substrate interface. Figure 8(c) further illustrates the flow of material from the central and peripheral portions of the stud as hypothesised

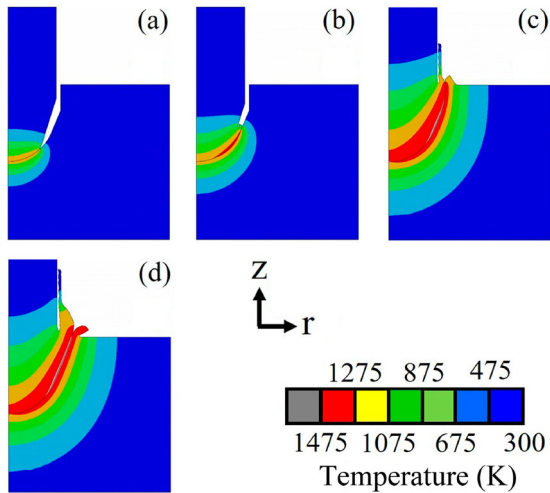


Figure 7. Temperature isotherms at stud burn-off length (mm) of (a) 0.5, (b) 2, (c) 6, and (d) 7 during the stud burn-off stage.

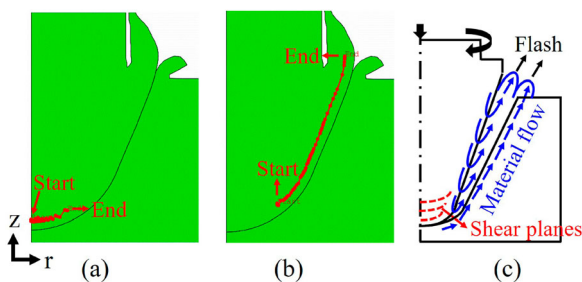


Figure 8. Distribution of tracer particles from (a) stud centre and (b) 4 mm away from the stud centre at the end of stud burn-off stage; and (c) schematic of material flow during FHPP.

based on the experimental investigation and modelling calculations. The material near the central portion of the stud would deform in a series of shear planes one upon the other, which are highlighted with the red colour dashed lines in Figure 8(c). This plastically deformed material remains inside the processed zone. The plastic flow of material from the tapered surface of the stud flown along the stud-hole contact interface in radially outward and upward direction and eventually the excess material expels as flash as shown in Figure 8(c). The model is validated further with the weld joint shape and flash size.

Figure 9(a,b) compares the measured profile of flash and joint cross-section with the corresponding computed results at two different process conditions. The measured joint cross-section in Figure 9(a) is from Figure 5(a) while that in Figure 9(b) is considered from literature [6]. In Figure 9(a,b), the original stud-substrate boundary is shown by the white dashed line that agrees well with the corresponding simulated flow of the tracer particles in both the cases. The profiles of the flash exiting out of the stud-substrate interface also indicate a fair correspondence between the model predictions and measures ones.

The material flow during FHPP of AISI 4140 was studied using Ti-6Al-4V as a tracer material. The

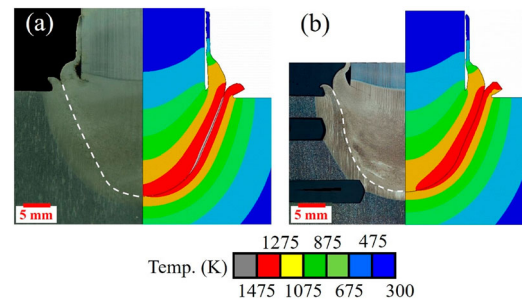


Figure 9. Computed and measured joint cross-sections and flash profiles at two different combinations of stud rotational speed (rev min^{-1}), stud force (kN) and stud burn-off (mm) of (a) (8000, 35, 7.0), and (b) (5000, 25, 6.5). Macrograph shown in Figure 9(b) is considered from independent literature [6].

tracer material distribution in FHPP joint was characterised by both XCT and metallographic analysis. A fully coupled temperature-displacement model was used to examine the evolution of material flow and temperature distribution as the externally rotating stud is introduced and forced to flow plastically to fill the crack-hole during the process. The XCT is proved to be a promising tool to visualise 3D material flow in typical solid-state joining processes involving flow of plasticised material. The experimental and numerical approaches presented here are fairly novel in nature for the analysis of FHPP that is increasing considered for joining of an external stud to a substrate for repairing of three-dimensional cracks.

Conclusions

A systematic investigation on material flow in FHPP is presented here based on novel experimental observation and comprehensive numerical modelling. The following conclusions are arrived at as a part of this detailed investigation.

- The material near the central portion of the stud plastically deformed in a series of shear planes one upon the other and this material remains inside the processed zone.
- The plastic flow of stud material from the taper surface flows in a radially outward and upward direction along the stud-hole interface, and eventually expelling as flash at the end of the stud burn-off.
- The thermal-displacement model developed in this study is first of its kind in FHPP literature and the computed peak temperature, material flow distribution, weld joint shape, and flash size and shape are fairly agreed well the corresponding XCT and metallographic results.

Acknowledgements

The authors would like to thank the research support of Petrobras, ANP (Brazilian Agency for Petroleum and Energy)

and General Electric. The authors are thankful to the late Professor T.R. Strohaecker (LAMEF/PPGE3M), whose presence and wisdom will be profoundly missed.

Disclosure statement

No potential conflict of interest was reported by the authors.

ORCID

Buchibabu Vicharapu  <http://orcid.org/0000-0003-2091-8022>

Amitava De  <http://orcid.org/0000-0002-3109-261X>

References

- [1] Meyer A. Friction hydro pillar processing – bonding mechanism and properties [master's dissertation]. Technical University Brunschweig; 2003.
- [2] Hattingh DG, Bulbring DLH, Els-Botes A, et al. Process parameter influence on performance of friction taper stud welds in AISI 4140 steel. *Mater Des.* 2011;32:3421–3430.
- [3] Yin Y, Yang X, Cui L, et al. Material flow influence on the weld formation and mechanical performance in underwater friction taper plug welds for pipeline steel. *Mater Des.* 2015;88:990–998.
- [4] Xu YC, Jing HY, Han YD, et al. Numerical simulation of the effects of various stud and hole configurations on friction hydro-pillar processing. *Int J Mech Sci.* 2015;90:44–52.
- [5] Vicharapu B, Kanan LF, Clarke T, et al. An investigation on friction hydro-pillar processing. *Sci Technol Weld Joining.* 2017;22:555–561.
- [6] Kanan LF, Vicharapu B, Bueno AFB, et al. Friction hydro-pillar processing of a high carbon steel: joint structure and properties. *Metall Mater Trans B.* 2018;49(2):699–708.
- [7] Thomas WM, Nicholas ED. TWI, leading edge. Friction hydro pillar processing. Cambridge: TWI Connect Press; 1992; [cited 2019 July 15]. Available from: www.twi.co.uk.
- [8] Meinhardt CP, Chudzinski M, Ribeiro RF, et al. Evaluation of friction hydro-pillar processing welding in duplex stainless steels (UNS S31803). *J Mater Process Technol.* 2017;246:158–166.
- [9] Zhang X, Deng C, Wang D, et al. Improving bonding quality of underwater friction stitch welds by selecting appropriate plug material and welding parameters and optimizing the joint design. *Mater Des.* 2016;91:398–410.
- [10] Bulbring DLH, Hattingh DG, Botes A, et al. Friction hydro-pillar processing as an alternative joining technology for the nuclear industry. *J S Afr Inst Min Metall.* 2015;113:903–912.
- [11] Cui L, Yang X, Wang D, et al. Friction taper plug welding for S355 steel in underwater wet conditions: welding performance, microstructures and mechanical properties. *Mater Sci Eng A.* 2014;611:15–28.
- [12] Maire E, Withers PJ. Quantitative X-ray tomography. *Int Mater Rev.* 2014;59:1–43.
- [13] Dialami N, Chiumenti M, Cervera M, et al. Material flow visualization in friction stir welding via particle tracing. *Int J Mater Form.* 2015;8:167–181.

- [14] Dinda SK, Warnett JM, Williams MA, et al. 3D imaging and quantification of porosity in electron beam welded dissimilar steel to Fe–Al alloy joints by X-ray tomography. *Mater Des.* 2016;96:224–231.
- [15] Kar A, Suwas S, Kailas SV. Two-pass friction stir welding of aluminum alloy to titanium alloy: a simultaneous improvement in mechanical properties. *Mater Sci Eng A.* 2018;733:199–210.
- [16] Krumm M, Kasperl S, Franz M. Reducing non-linear artifacts of multi-material objects in industrial 3D computed tomography. *NDT E Int.* 2008;41:242–251.
- [17] Meyer-Spradow J, Ropinski T, Mensmann J, et al. Voreen: a rapid-prototyping environment for ray-casting-based volume visualizations. *IEEE Comput Graph Appl.* 2009;29(6):6–13.
- [18] ABAQUS analysis user's manual. Chapter 6 – heat transfer and thermal-stress analysis.
- [19] Moal A, Massoni E. Finite element simulation of the inertia welding of two similar parts. *Eng Comput.* 1995;12:497–512.
- [20] ABAQUS Example problems guide. Example number 1.3.18 inertia friction welding.
- [21] Buchibabu V, Reddy GM, De A. Probing traverse force, torque and tool durability in friction stir welding of aluminum alloys. *J Mater Process Technol.* 2017;241:86–92.
- [22] Vicharapu B, Liu H, Fujii H, et al. Probing tool durability in stationary shoulder friction stir welding. *Frict Stir Weld Process X.* 2019: 91–98. DOI:10.1007/978-3-030-05752-7_9.
- [23] Agmell M, Ahadi AS, Ståhl J-E. The link between plasticity parameters and process parameters in orthogonal cutting. *Procedia CIRP.* 2013;8:224–229.
- [24] Meyer HW, Kleponis DS. Modeling the high strain rate behavior of titanium undergoing ballistic impact and penetration. *Int J Impact Eng.* 2001;26:509–521.

Appendix

Table A1 provides the Johnson-Cook model constants for Ti–6Al–4V. Figure A1 compares the flow stress between Ti–6Al–4V and the AISI 4140 steel as function of (a) temperatures, and (b) equivalent plastic strains. Figure A1 shows that the flow stress of AISI 4140 and Ti–6Al–4V is reasonably close to each-other.

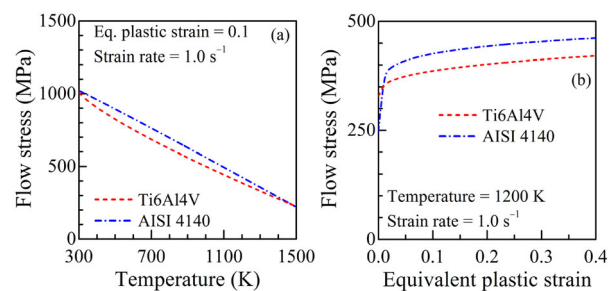


Figure A1. A comparison of flow stresses for AISI 4140 and Ti–6Al–4V as function of (a) temperatures, and (b) equivalent plastic strains.

Table A1. Johnson-Cook model constants for tracer [24].

Material	A (MPa)	B (MPa)	C	M	N	T_M (K)
Ti–6Al–4V	862.5	331.2	0.012	0.8	0.34	1941